LES Study into the Flow Physics of an Undulating Leading-Edged Wing

ERCOFTAC international symposium «Unsteady separation in fluid-structure interaction» Mykonos, Greece, June 17-21, 2013

LES Study into the Flow Physics of an Undulating Leading-Edged Wing

A Skillen[1], A Revell[1], J Favier[2], A Pinelli[3], U Piomelli[4]

[1]*Modelling and Simulation Centre, School of MACE, The University of Manchester, UK*
[2]*Laboratoire de Mécanique, Modélisation et Procédés Propres (M2P2), Aix-Marseille Université, UMR7340 CNRS, 13451 Marseille, France*
[3]*School of Engineering and Mathematical Science, City University London, UK*
[4]*Dept. of Mechanical and Materials Engineering, Queen's University, Kingston (Ontario) K7L 3N6, Canada.*

Abstract.

We present LES simulations of the flow over a wing with sinusoidal leading edge undulations. The undulations act as a passive flow control device, offering superior post-stall aerodynamic performance relative to the unmodified wing with the same mean chord. The effect of the undulation's geometrical parameters on the flow physics is explored. A total three different geometrical configurations are investigated. Comparisons against the baseline unmodified wing are also presented. In all cases the Reynolds number based on bulk velocity and mean chord is equal to $120,000$, and the angle of attack is set to $20°$.

1 Introduction

Inspired by the high maneuverability of the humpback whale, there has been a surge in interest in the mammal's hydrodynamic performance, with a view towards capitalising on findings in the field of biomimetics. A key contributing factor to this high maneuverability is the form of the pectoral flippers; specifically the presence of protuberances (or undulations) along the leading edge, which act as a passive flow control device delaying separation.

Several attempts have been made to elucidate the physical mechanisms by which the undulations offer their benefit. Fish et al. [1] present a morphological study and suggest the undulations act as vortex generators, re-energising the boundary layer. They also suggest the undulations may increase the effective span of a finite wing by diminishing the spanwise flow component, thereby reducing the strength of the wing-tip vortex. Stanway [2] performed PIV measurements around a finite wing with protuberances. Pairs of vortical structures were observed emanating from each protuberance. Stanway suggests a physical mechanism similar to that of a delta wing, whereby chord-wise vortices generate lift.

Favier et al. [3] conducted numerical simulations of an undulating geometry at $Re = 800$ and an angle of attack of $20°$. A parametric study was performed on the undulations, covering a range of wavelengths and amplitudes. While the authors observed a peak drag reduction of 35%, the lift was also reduced relative to the baseline unmodified case for all configurations. This inauspicious result is likely to be a consequence of the low flow Reynolds number considered (several orders of magnitude lower than that observed in nature, and lower than that required for transition to turbulence). In the study, a Kelvin-Helmholtz-like instability was identified, driven by the spanwise modulation of the streamwise velocity component, induced by the undulations. It was reasoned that this instability acts to produce rolls of vorticity emanating from the undulation site. The rolls,

initially vertical, are then tilted into the streamwise direction as they are advected by the flow. The vortices decrease drag by acting on boundary-layer separation and promoting attachment.
Miklosovic et al. [4] performed wind tunnel measurements on both infinite and finite wings with an undulating leading edge. They found a significant performance decrease for the infinite wing relative to their finite span model, leading to the suggestion that the protuberances gained their benefit via interaction with the wing tip vortices, and that the benefit would be best realised in the case of a finite wing. However, it must be noted that in their study, the operating Reynolds number for the infinite case was less than half that of the finite span. Stanway [2] showed a strong sensitivity of the performance enhancement to the flow Reynolds number, thereby casting doubt over the proposed significance of the wing tip vortices.
Hansen et al. [5] performed a series wind tunnel measurements over sinusoidal undulating geometries, covering a wide range of wavelengths and amplitudes. The study also considered both finite and infinite wing configurations, all at $Re = 120,000$. The authors show that both the finite and infinite configurations offered a similar performance benefit, further indicating that the wing tip effect is not as significant as originally thought.
While some insight has been gained into the principal flow mechanisms, a detailed flow physics investigation has not been provided thus far. Specifically, while the performance benefit has been quantified in terms of the integral quantities for a range of different wavelengths and undulation amplitudes [5], the effect of these parameters on the flow physics is unclear. Moreover, the effect of Reynolds number on the flow physics has not been explored in any great detail. While it is generally accepted that the undulations induce a vortex system, there is no general consensus over the mechanisms by which this vortex is driven; indeed it may be the case that fundamentally different mechanisms are involved for different geometrical configurations and flow Reynolds numbers.
In the present study, we outline LES calculations of the flow over a wing with sinusoidal leading edge undulations. A total of three different undulating geometries are considered. The flow Reynolds number based on mean chord length and bulk velocity is $120,000$, and the incidence angle is set to $20°$. It will be shown that under these conditions, the main physical mechanism involved originates from a secondary flow induced by the undulations. This secondary flow acts to transport low momentum fluid from behind the chord peak, thereby re-energising the boundary layer, which reduces the size of the separated region. The reduction in the size of the separated region presents a favourable effective aerodynamic form (relative to the baseline case of a wing without undulations at the same angle of attack and flow conditions), thereby significantly improving aerodynamic performance.

2 Numerical approach

The filtered incompressible Navier Stokes equations govern the flow development;

$$\begin{aligned} &\frac{\partial \overline{u}_i}{\partial t} + \frac{\partial}{\partial x_j}\left(\overline{u}_i \overline{u}_j\right) = \\ &\qquad \frac{\partial}{\partial x_j}\left[-\overline{p}\delta_{ij} + \nu\left(\frac{\partial \overline{u}_i}{\partial x_j} + \frac{\partial \overline{u}_j}{\partial x_i}\right) - \tau_{ij}\right] \\ &\frac{\partial \overline{u}_i}{\partial x_i} = 0 \end{aligned} \tag{1}$$

where an overbar denotes a filtered field, and τ_{ij} is the residual stress tensor. The filtering operation is performed implicitly by the mesh.
Equations 1 are closed via an eddy viscosity model;

$$\tau_{ij} = -2c_s\Delta^2 \left|\overline{S}\right| \ \overline{S}_{ij} \tag{2}$$

where $\overline{S}_{ij}$ is the resolved strain rate tensor, $\left|\overline{S}\right| = \sqrt{2\overline{S}_{ij}\overline{S}_{ij}}$, and Δ is the local filter width, taken as $V^{1/3}$ (where V is the cell volume). The model constant $c_s\left(\mathbf{x}, t\right)$ is set according to the Germano-Lilly dynamic procedure [6, 7].

Table 1: Geometries considered

Label	$\lambda/\overline{c}$	$A/\overline{c}$	λ/A
Unmodified	∞	0	∞
L11A015	0.11	0.015	7.3
L21A015	0.21	0.015	14
L21A030	0.21	0.03	7

The governing equations are discritised via the Finite volume method. We use a central scheme for the interpolation of face values in convective and viscous flux terms. For temporal discritisation, a second order implicit scheme is used. A temporally varying time-step size is used, set to yield a maximum global Courant number of unity. Pressure velocity coupling is achieved via the PISO algorithm.

The discritised equations are solved iteratively using the OpenFOAM package until first and second order statistics are fully converged. Statistics are gathered over 400 dimensionless time units (defined as $t' \equiv Ut/\overline{c}$, where U is the bulk velocity, t and t' are the physical and dimensionless times respectively, and $\overline{c}$ is the mean chord). The initial transient phase does not contribute towards the statistics.

3 Geometry and mesh

Figure 1 shows a typical undulating geometry used in the present study. A NACA 0021 wing section is employed and is set at an angle of attack of 20°; a post-stall condition. The chord length for the undulating cases varies as:

$$c(z) = A\cos\left(\frac{2\pi z}{\lambda}\right) + \overline{c} \tag{3}$$

where A is the amplitude of the undulation, λ is the wavelength of the undulation, and z is the spanwise ordinate. We consider a total of three undulating geometries with amplitudes and wavelengths set out in table 1. The baseline unmodified NACA 0021 profile is also computed for comparison.

The extents of the computational domain reach $10\overline{c}$ upstream of the leading edge, and $15\overline{c}$ downstream of the trailing edge. Lateral boundaries are placed $15\overline{c}$ from the wing. The extent of the domain in the spanwise direction is set at $0.42\overline{c}$ and $0.44\overline{c}$ for the $\lambda = 0.21\overline{c}$ and $\lambda = 0.11\overline{c}$ cases respectively (corresponding to two or four wavelengths of the undulation). An extent of $0.44\overline{c}$ is also used for the unmodified case. The spanwise extent of the domain has been set so as ensure that the two-point correlation is sufficiently decorrelated by the edge of the domain to have confidence that the correct underlying physics is captured. Tests with a reduced spanwise extent (not presented) have revealed no differences to the primary physical mechanisms at play.

Meshes comprising around 3.5×10^7 cells have been used, with around $150,000$ cells in each xy-plane. All meshes are of block-structured hexahedral topology, with a 'C-shape' grid being wrapped around the wing. The same mesh density in the xy-plane is used for all cases, with the mesh being smoothly adjusted to conform to the contour of the geometry at the undulation site. Near wall cells are placed at $y^+ < 1$ in all cases. Between 5 and 10 computational cells occupy the near-wall region $y^+ < 10$, depending on the local flow conditions. The grid spacing in terms of wall units is $\Delta x^+ < 30$ and $\Delta z^+ < 15$ at all relevant locations at the wall. Grid sensitivity tests have been conducted with cell counts around 50% lower than that presented herein. No fundamental differences to the physical mechanisms involved were observed at the reduced cell count (though the quantitative results for the integral quantities did differ by a few per cent).

Table 2: Mean lift and drag coefficients

	$\langle CL \rangle$	$\langle CD \rangle$
Unmodified	0.63	0.33
L21A030	0.94	0.21
L21A015	1.06	0.16
L11A015	1.05	0.12

4 Boundary conditions

A uniform velocity is applied at the inlet, with zero free-stream turbulence. Lateral boundaries are modelled as slip walls. At the outlet, a zero pressure condition is employed, while periodicity is applied in the spanwise direction. The wing surface is modelled as a non-slip wall with zero surface-velocity and a zero gradient condition in the wall-normal direction for the surface pressure. No special treatment is required at the wall since the grid is sufficiently fine to resolve fully the fluid boundary layer. Moreover, the dynamic sub-grid model employed is known to give correct asymptotic behaviour on approaching a solid surface without the need for damping functions.
It is expected that there will be a sensitivity of the flow to the incoming turbulence levels. However, such an investigation is left as future work.

5 Results

Figure 2 shows the time history of lift coefficient for all cases. Table 2 shows the time-averaged force coefficients. It can be seen that the undulating geometries consistently yield a significant increase in lift, and a decrease in drag relative to the unmodified geometry, though the magnitude of the benefit varies with the geometrical parameters. In Figure 3, phase-space plots of the instantaneous force coefficients are presented. From this, it is apparent that for the L11A015 case, the variance in force coefficients is minimal, indicating a suppression of vortex shedding. Conversely, the region in phase-space traced by the L21A030 case is enlarged relative to the unmodified geometry; this is generally undesirable since a large variance in the force coefficients can lead to issues in terms of noise production, structural integrity (due to vortex induced vibrations), and control.
Figure 4 shows the Fourier transform of the time-dependent lift coefficient. From the figure, it is apparent that the vortex shedding frequency for the unmodified case is at a Strouhal number of around 0.57. No frequency peak is recorded for the L11A015 case, thereby confirming the almost complete suppression of the vortex shedding discussed above. For the L21A030 and L21A015 cases, low frequency peaks are observed, which are thought to be associated with an intermittent asymmetric alternation of the flow; while the time-averaged mean flow is symmetric about chord normal planes (e.g. through the chord peak), the ensemble average is not necessarily so. It is possible that interactions between the wakes of the undulations themselves are behaving in a similar way to that observed for the flow over two side-by-side cylinders (e.g. [8]), with phase locking for small λ, and a bi-stable alternation for the larger λ cases. Further investigation is required to confirm this.
Figure 5 shows the iso-surface of zero streamwise velocity component for all the cases, indicating the size of the separated region. In all cases, broadly similar patterns are observed, the details of which shall be discussed later. For now, the most note-worthy feature is that the size of the separated region is reduced in all modified cases relative to the unmodified geometry. The reduced size of the separation region explains the improved aerodynamic performance since a superior effective aerodynamic shape is achieved. The observed mechanism by which there is a reduction in separation region size is elucidated as follows:

- Oncoming flow is deflected by the leading-edge geometry such that the bulk of the flow is directed behind the chord minima (see Figure 6).
- Strong flow acceleration behind the minima results, with a consequential local augmentation of the suction peak, resulting in the formation a spanwise pressure gradient (Fig. 7).

- This spanwise pressure gradient drives the development of a secondary flow whereby low-inertia boundary-layer fluid is transported from behind the chord maxima, towards the minima (Fig. 8).
- The low-inertia fluid is replaced by high momentum fluid drawn from above, thereby re-energising the boundary layer, delaying separation behind each chord peak.
- This mechanism is apparent across the range of geometries considered herein, as can be seen from Figures 9, 10 and 11 which show the wall shear stress for the L21A030, L21A015, and L11A015 cases respectively (this mechanism is observed near to the leading edge).

Figure 12 shows profiles of the wall shear stress behind both the chord maxima and minima. From Figure 12a, it is apparent that the flow separates (for all cases) a short distance downstream of the leading edge behind the chord minima. The enhanced suction peak downstream of the chord minima, combined with the reduced local chord length, leads to a large adverse pressure gradient, and ultimately a laminar separation close to the leading edge behind each chord minima. For the L21A030 and L11A015 cases, this initial separation is restricted to the region behind the chord minima. For the L21A015 case, however, the separation extends across the entire span (see Figures 5 and 10). Since the ratio $\frac{\lambda}{A}$ for the L21A015 case is large (relative to the other two modified geometries), the geometry is closer to that of the unmodified case, and hence the affect of the undulations is reduced. The re-energisation of the boundary layer by the secondary flow is therefore less pronounced, and hence the boundary layer separates.
For all cases, transition is observed to occur in the separated shear layer (behind the minima) due to the amplification of perturbations via the Kelvin-Helmholtz mechanism (see Figure 13). Subsequent to this, momentum transfer due to turbulent mixing quickly reattaches the shear layer in the L21A015 and the L11A015 cases, at which point the fluid bifurcates into a laminar separation bubble and a newly energised boundary layer upstream and downstream of the reattachment point respectively. For the L21A030 case, however, the extent of the flow deflection by the undulations (and hence the strength of the secondary flow) is sufficiently great so as to allow the secondary flow feature to persist well downstream of the leading edge; this dominates over any reattachment behind the minima that would otherwise occur, and hence the flow remains separated behind the chord minima all the way to the trailing edge.
For cases L11A015 and L21A015, vortex systems are generated, (see Figures 11 and 10 respectively). The vortices are driven primarily by viscous shear interaction between the streamwise flow behind the chord peak, and the low inertia reversed flow in the recirculation zone. It is possible the vortices act to regulate the size of the recirculation zone across the span since the feature acts to transport momentum from behind the chord maxima to behind the minima (particularly for case L21A015 where the vorticies are larger), though it must be noted that the energy contained in this vortex system is relatively low (the shear stress is low, see Figure 12), and hence it should have a comparatively small effect on the mean flow.

6 Conclusion

Wall-resolved LES simulations are presented for the flow over a NACA 0021 wing with leading edge undulations. A total of three different undulating geometries are considered. For the best performing case,a 66% increase in mean lift and a 64% decrease in mean drag is observed. It is observed that this performance enhancement arises since size of the separated zone is significantly reduced (relative to that of the standard NACA 0021 wing), thereby yielding a superior effective aerodynamic shape.
The mechanisms by which the size of the separation zone is reduced are explored. It is shown that the undulations induce a strong spanwise pressure gradient due to the fact that the bulk of the oncoming flow is redirected behind the chord minima. This spanwise pressure gradient induces a secondary flow; low inertia boundary-layer fluid from behind the peak chord is transported in the spanwise direction toward the suction peak. High momentum fluid from above replaces the boundary-layer fluid, thereby re-energising the boundary layer behind the chord maxima, delaying separation. This mechanism is consistent across the three undulating geometries considered. This

observed mechanism by which the undulations offer their aerodynamic benefit is significantly different to the speculative ideas proposed in e.g. [1, 2]. It is also significantly different to that observed at low Reynolds numbers [3], though there may be an element of the Kelvin-Helmholtz-driven mechanism contributing here.

Acknowledgement

This work made use of the facilities of HECToR, the UK's national high-performance computing service, which is provided by UoE HPCx Ltd at the University of Edinburgh, Cray Inc and NAG Ltd, and funded by the Office of Science and Technology through EPSRC's High End Computing Programme.
The work also made use of the facilities of N8 HPC, provided and funded by the N8 consortium and EPSRC (Grant No.EP/K000225/1). The Centre is co-ordinated by the Universities of Leeds and Manchester.
AP was partially supported by the Spanish Ministry of Economy and Competitiveness through the grant INFIESMED
UP acknowledges the support of the NSERC Discovery Grant program.

References

[1] Frank E Fish, Paul W Weber, Mark M Murray, and Laurens E Howle. The tubercles on humpback whales' flippers: application of bio-inspired technology. *Integrative and comparative biology*, 51(1):203–13, July 2011.

[2] Michael Jordan Stanway. *Hydrodynamic effects of leading-edge tubercles on control surfaces and in flapping foil propulsion.* PhD thesis, MIT, 2008.

[3] Julien Favier, Alfredo Pinelli, and Ugo Piomelli. Control of the separated flow around an airfoil using a wavy leading edge inspired by humpback whale flippers. *Comptes Rendus Mécanique*, 340(1-2):107–114, January 2012.

[4] David S. Miklosovic, Mark M. Murray, and Laurens E. Howle. Experimental Evaluation of Sinusoidal Leading Edges. *Journal of Aircraft*, 44(4):1404–1408, July 2007.

[5] K L Hansen, R M Kelso, and B B Dally. Performance Variations of Leading-Edge Tubercles for Distinct Airfoil Profiles. *AIAA Journal*, 49(1):185–194, 2011.

[6] Massimo Germano, Ugo Piomelli, Parviz Moin, and William H Cabot. A dynamic subgrid-scale eddy viscosity model. *Physics of Fluids A: Fluid Dynamics*, 3:1760, 1991.

[7] DK Lilly. A proposed modification of the germano subgrid-scale closure method. *Physics of Fluids A: Fluid Dynamics*, 4:633, 1992.

[8] ZJ Wang and Y Zhou. Vortex interactions in a two side-by-side cylinder near-wake. *International journal of heat and fluid flow*, 26(3):362–377, 2005.

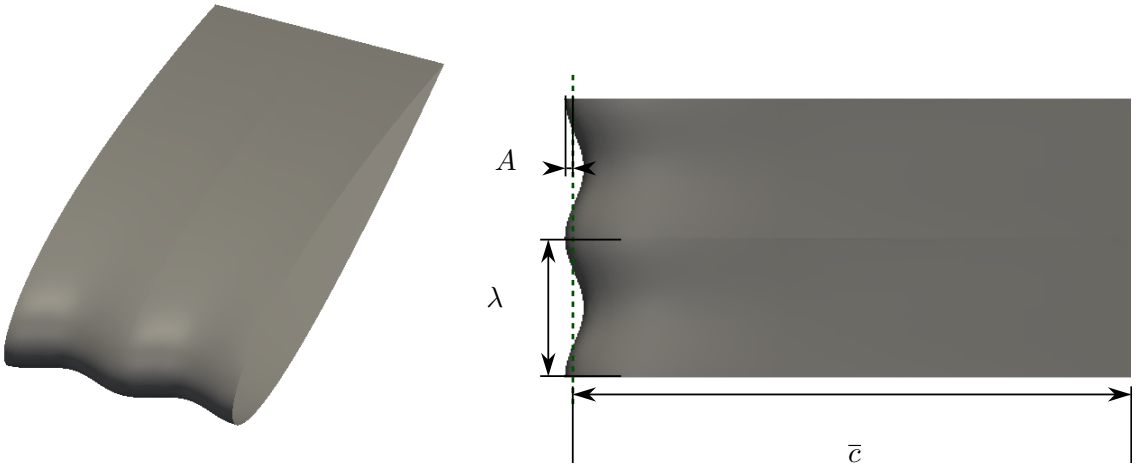

Figure 1: Typical geometry considered

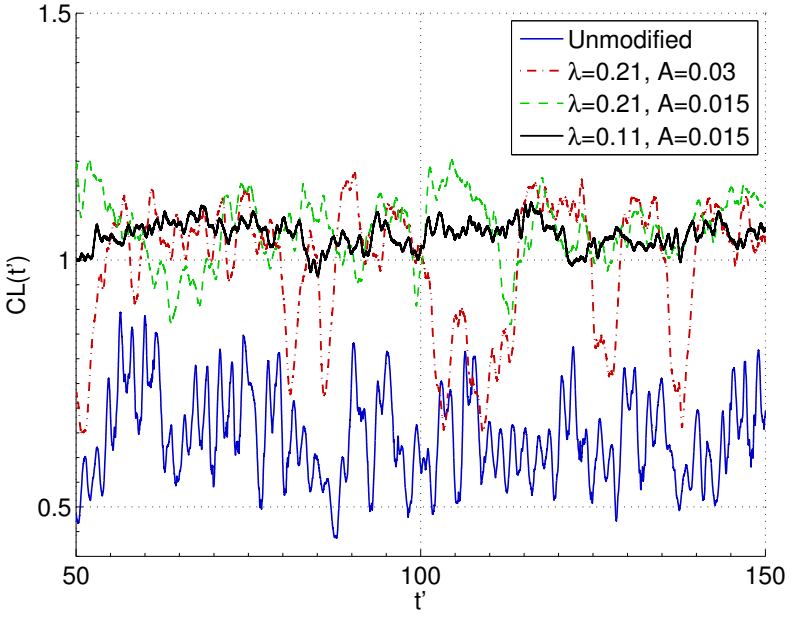

Figure 2: Instantaneous lift coefficient for all geometries.

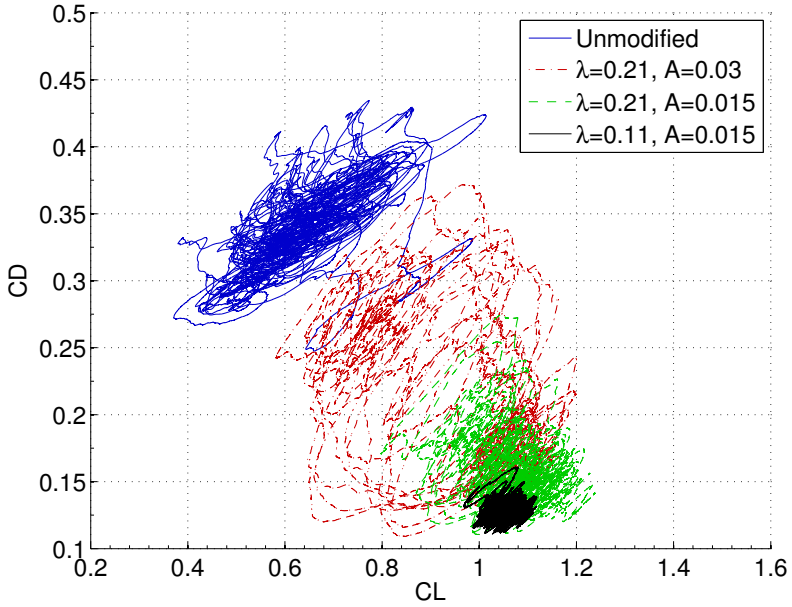

Figure 3: Phase-space plot of instantaneous force coefficients for all geometries.

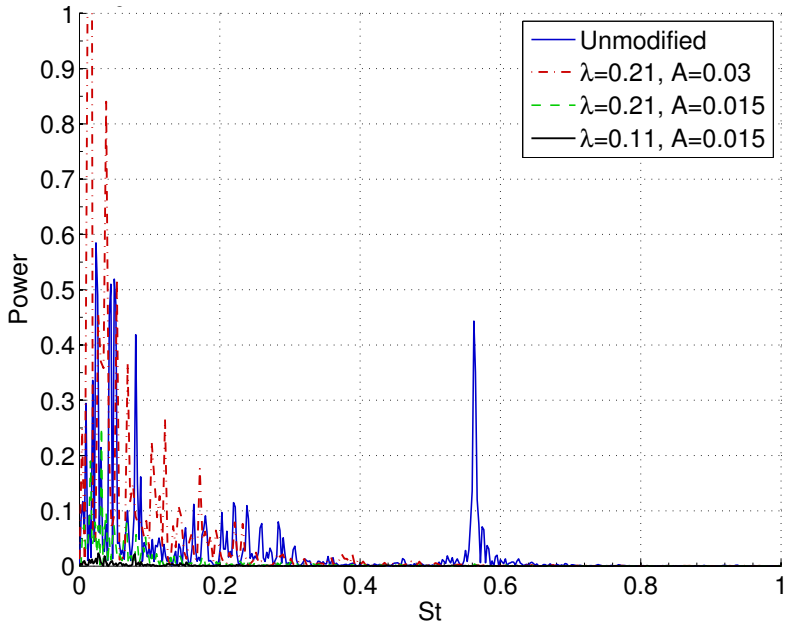

Figure 4: Fourier transform of the time-dependent lift coefficient.

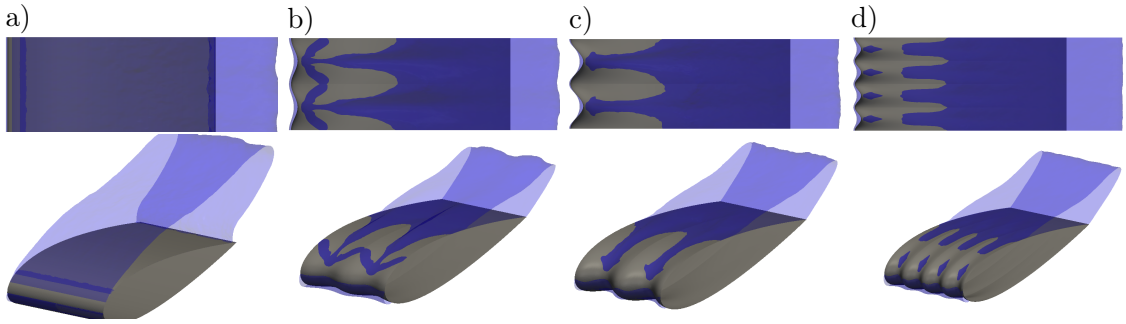

Figure 5: Iso-surface of zero streamwise time-average velocity. Plan view (above). 3D view (below). a) unmodified b) L21A015 c) L21A030 d) L11A015

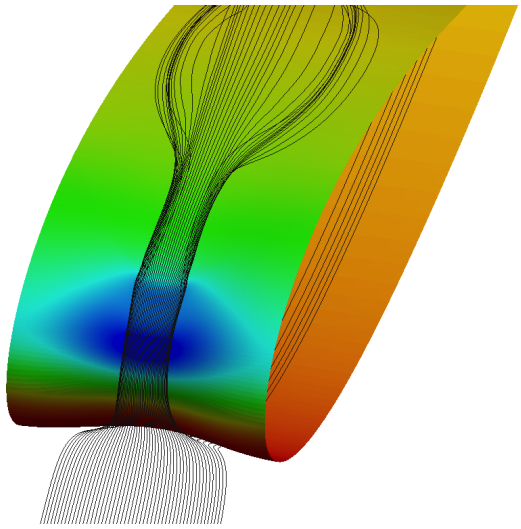

Figure 6: Time averaged streamlines showing deflection on oncoming flow at the leading edge region. Half span shown for clarity. Colour pressure (blue to red).

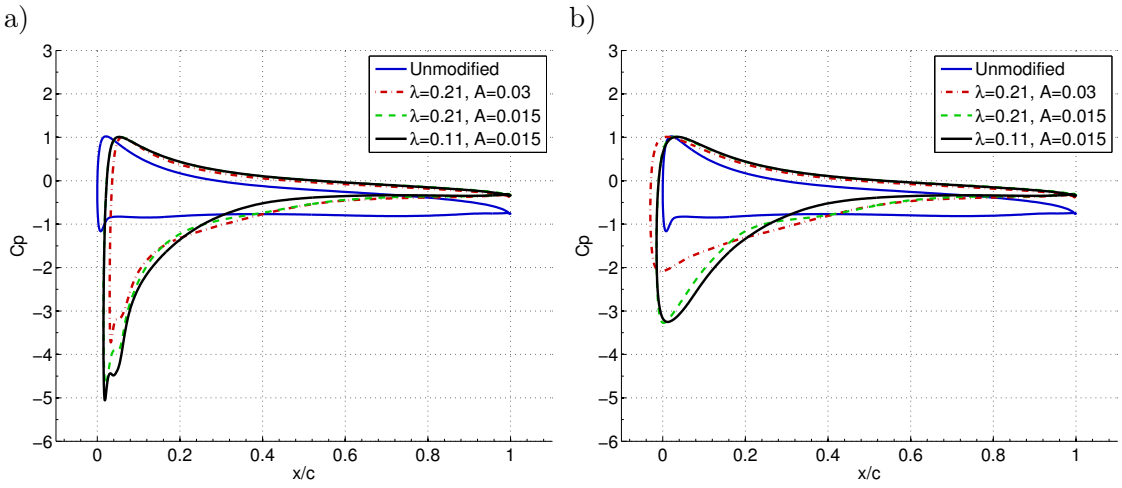

Figure 7: Surface pressure coefficient. a) Behind chord minima. b) Behind chord maxima

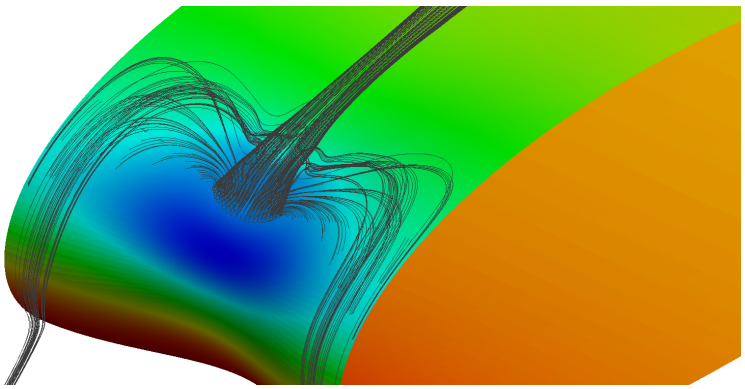

Figure 8: Time averaged streamlines showing secondary flow feature. Half span shown for clarity. Colour pressure (blue to red).

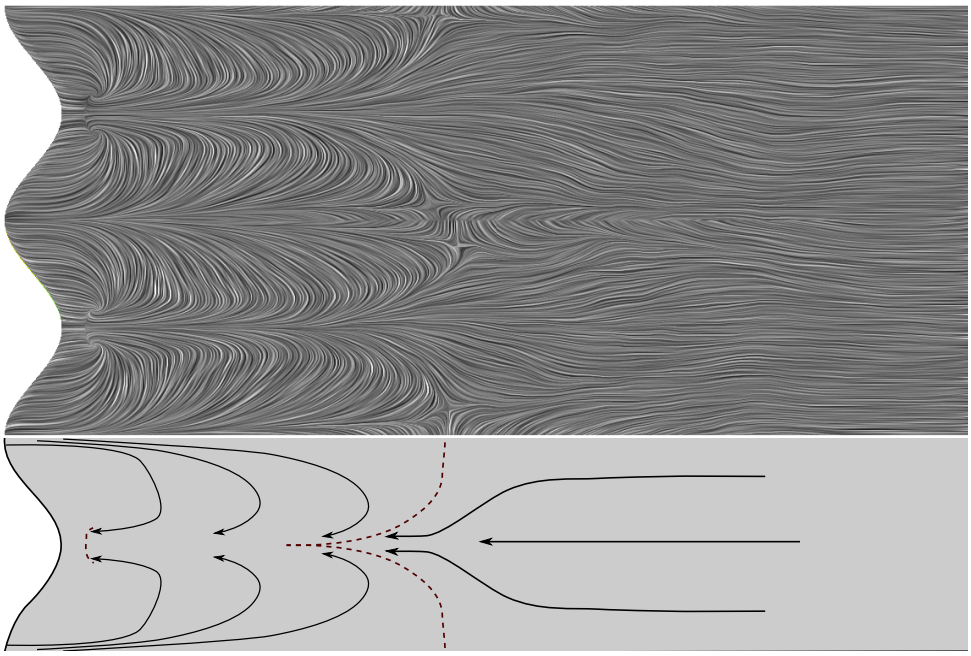

Figure 9: Time-average wall shear stress for L21A030 case visualised with the line integral convolution technique (above). Sketch showing flow direction (arrows), and separation lines (red dashed) (below).

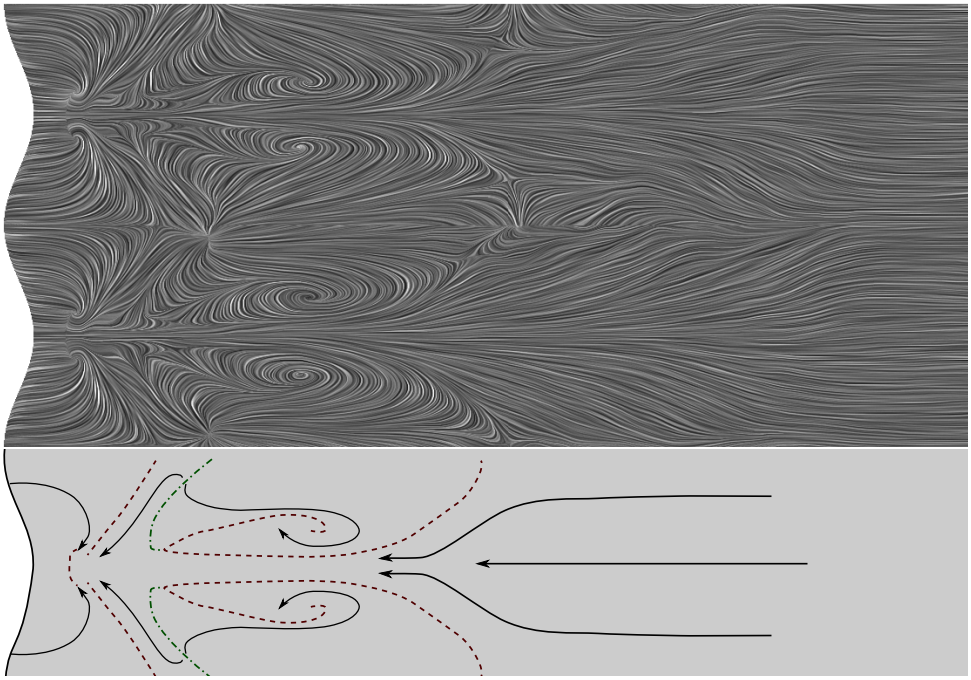

Figure 10: Time-average wall shear stress for the L21A015 case visualised with the line integral convolution technique (above). Sketch showing flow direction (arrows), separation lines (red dashed), and reattachment lines (green dot-dash) (below).

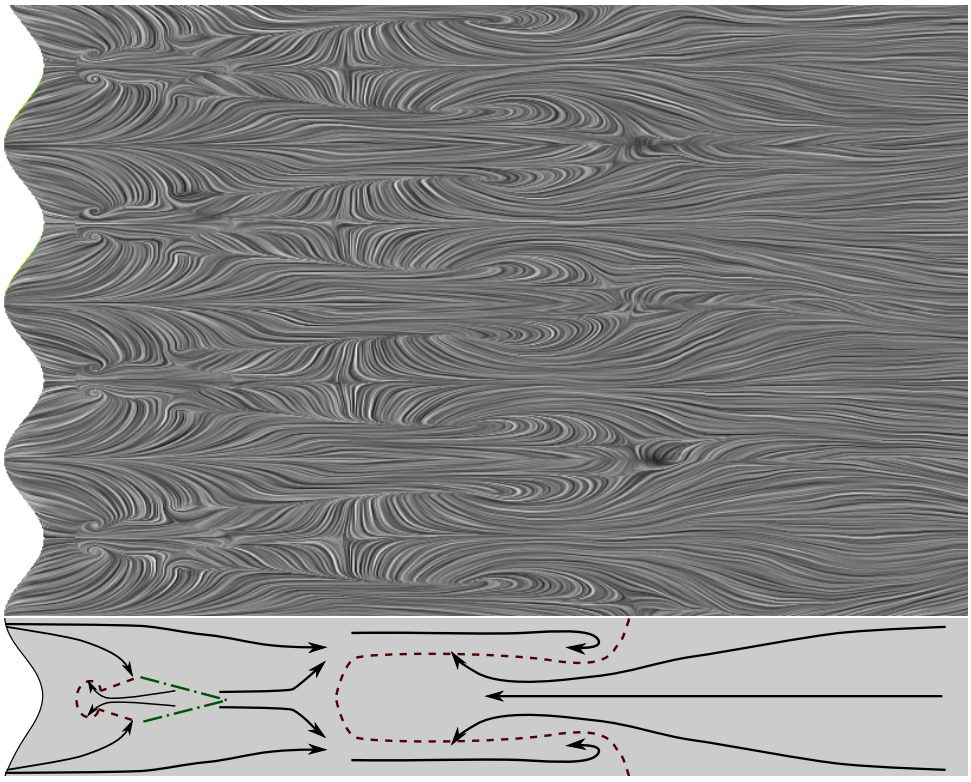

Figure 11: Time-average wall shear stress for the L11A015 case visualised with the line integral convolution technique (above). Sketch showing flow direction (arrows), separation lines (red dashed), and reattachment lines (green dot-dash) (below).

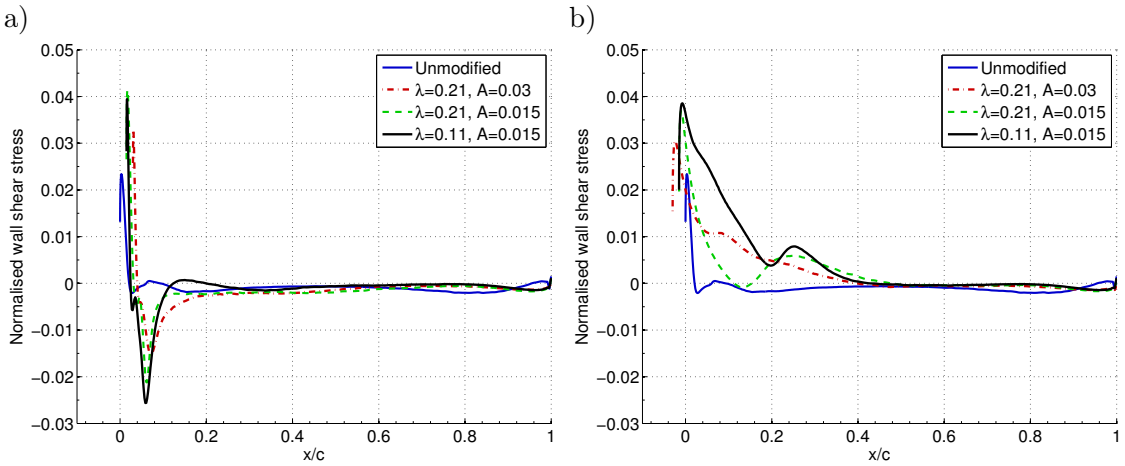

Figure 12: Streamwise component of time-averaged skin friction. a) Behind chord minima. b) Behind chord maxima

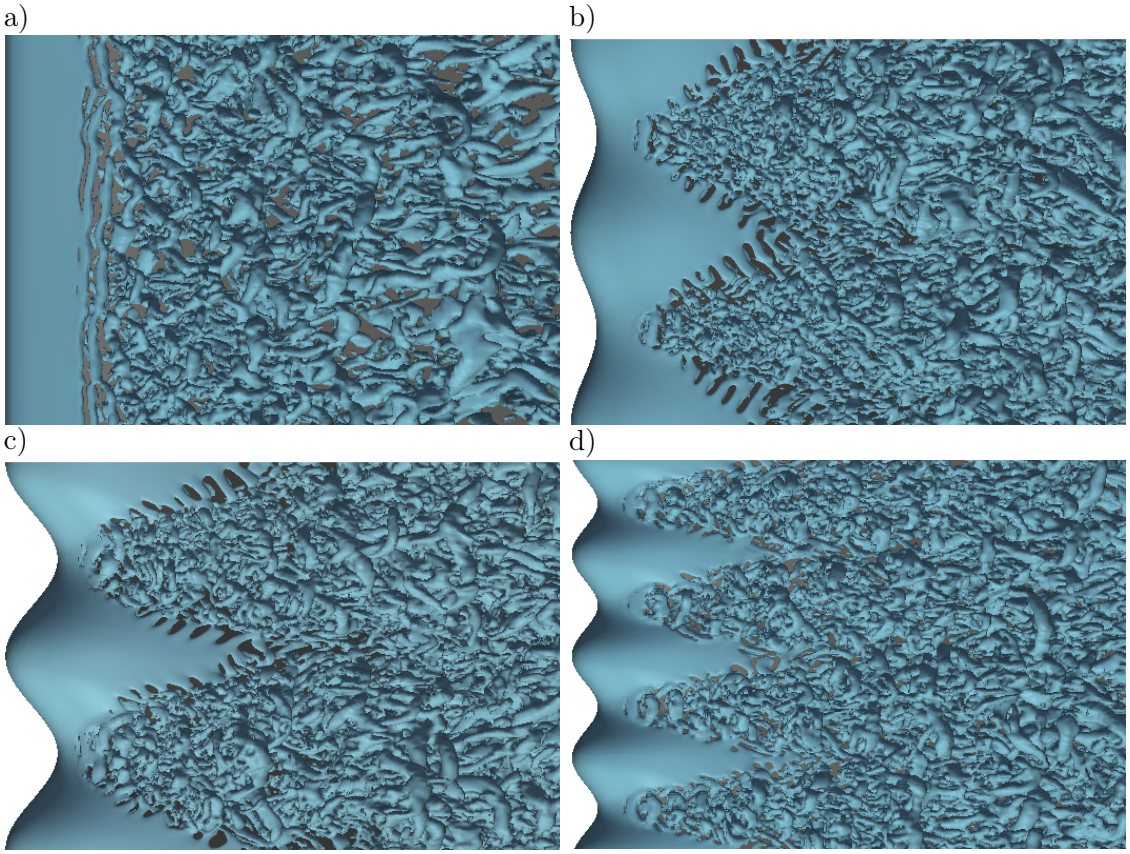

Figure 13: Iso-surfaces of Q=200. a) unmodified b) L21A015 c) L21A030 d) L11A015